Optics & Laser Technology 204 (2026) 116162

Contents lists available at ScienceDirect

Optics and Laser Technology

journal homepage: www.elsevier.com/locate/optlastec

Full length article

Measurement of beam attenuation by the vapor plume during full-penetration laser welding of stainless steel, aluminum and copper

Johannes Wahl [a,*], Christian Frey [b], John Powell [a], Simon Olschok [b], Uwe Reisgen [b], Christian Hagenlocher [a], Thomas Graf [a]

[a] Institut für Strahlwerkzeuge (IFSW), University of Stuttgart, Pfaffenwaldring 43, 70569 Stuttgart, Germany
[b] Welding and Joining Institute (ISF), RWTH Aachen University, Pontstraße 49, 52062 Aachen, Germany

ARTICLE INFO

Keywords:
Laser welding
Vapor plume
Laser beam absorption
Laser beam scattering
Laser beam attenuation

ABSTRACT

During deep-penetration laser welding, the associated vapor plume attenuates the laser beam through scattering and absorption, resulting in a reduction of laser power contributing to the welding process. In the present study, the attenuation of the laser beam was measured in detail for stainless steel, aluminum, and copper under various atmospheric conditions. To achieve this, a novel beam configuration is employed, in which a coaxially aligned probe laser beam propagates along the same path as the processing laser beam through the interaction zone and the bottom opening of the keyhole during full-penetration welding. After separation from the residual processing beam, the laser power of the transmitted probe beam was measured using an integrating sphere and a photodiode. The results show that the attenuation was highest for stainless steel, followed by copper, and then aluminum. For all three materials, the attenuation occurred primarily within the keyhole and in its immediate vicinity. Furthermore, in the overall attenuation resulting from absorption and scattering, absorption was identified as the dominant effect. Mie–theory calculations for single–particle interactions matched the measured attenuation, confirming the experimental findings. Finally, lowering the ambient pressure noticeably reduced the total attenuation.

1. Introduction

Laser welding is an essential technology in modern manufacturing due to its high processing speed, precision, and capacity for remote operation. In deep-penetration laser welding, a high-intensity laser beam is focused on the material's surface, creating a vapor-filled capillary, or keyhole, by vaporizing a portion of the metal. This keyhole enhances the radiation coupling between the laser beam and the material, significantly increasing the overall efficiency of the process. However, some of the vaporized metal escapes from the keyhole, forming a plume above the keyhole opening. This plume can interfere with the incident laser beam, adversely impacting the process. In remote laser welding, inadequate plume removal often results in a wider, shallower weld seam, which compromises weld quality and stability [1].

The properties of the vapor plume above the keyhole depend on numerous factors, including the material being welded and the wavelength of the processing laser. For instance, when using high-power CO_2 lasers, the ionized metal vapor absorbs a substantial amount of laser power by inverse bremsstrahlung, generating a high-temperature plasma in the keyhole and its immediate surroundings [2]. In contrast, the radiation of solid-state lasers, like fiber or thin-disk lasers operating in the near-infrared (NIR) range, exhibits reduced interaction with metal vapor due to their significantly shorter wavelength (~ 1 μm), leading to a cooler, weakly ionized plume [3,4]. As the plume rises above the keyhole and cools, particles begin to form through nucleation and condensation. The scattering and absorption of laser energy by these particles in the unsteady plume leads to a fluctuating attenuation of the laser intensity reaching the material surface. The interaction between keyhole dynamics and plume interference was initially highlighted by Matsunawa et al. [5] and has since been widely investigated. Research on the links between the influence of the plume and melt pool dynamics includes studies by Fabbro et al. and Volpp et al. [6–8]. These works demonstrated that spatter and particle ejection from the melt pool are closely linked to the interactions between the ejected vapor and the molten material. Recent studies of Yang et al. and Zhu et al. [9,10] covered a numerical analysis on vapor plume and capillary interactions,

* Corresponding author.
E-mail address: johannes.wahl@ifsw.uni-stuttgart.de (J. Wahl).

https://doi.org/10.1016/j.optlastec.2026.116162
Received 11 March 2026; Received in revised form 29 June 2026; Accepted 10 August 2026
Available online 15 August 2026
0030-3992/© 2026 The Author(s). Published by Elsevier Ltd. This is an open access article under the CC BY license (http://creativecommons.org/licenses/by/4.0/).

revealing a coupled relationship of capillary fluctuations and the probability of capillary collapses and the dynamic behavior of the plume. Experimental investigations from Kawahito et al. [4,11], provided insights into plume formation and characteristics, employing high-speed imaging and spectroscopic analysis to assess the influence on keyhole stability. Furthermore, spectrometer measurements were used to estimate prevailing temperatures in different regions of the plume, using the Boltzmann-plot method and Saha's equation [3,4,12]. These spectroscopic analyses revealed a temperature gradient along the laser beam axis, with the highest temperatures located near the keyhole.

Extinction[1] or attenuation measurements, typically obtained by aligning a secondary probe beam transversally with respect to the processing beam, have provided spatially resolved data on the plume's overall extinction coefficient [1,11,14–18]. By using the multi-wavelength method, researchers have estimated particle sizes within the plume [1,3,15,19], which range from roughly 2 nm to 200 nm, as confirmed by Transmission Electron Microscopy (TEM) analyses [12,17,20]. In some cases, agglomeration can lead to particle sizes exceeding one micron. However, particle size distributions vary, depending on material, weld parameters, and environmental factors such as ambient pressure and gas type, which influence oxidation and size evolution. The size and oxidation state of the particles define the optical properties of the plume according to Mie theory and therefore influence laser scattering and absorption [13]. Hansen and Duley's research [21], using Mie calculations and estimates on evaporation time, suggests that tiny condensed particles or aerosols from the melt pool may persist even within the keyhole region. They suggest that the intense laser energy drives a dynamic cycle of nucleation, condensation, and re-evaporation within the plume, resulting in significant laser attenuation. Our previous research [22,23] supports this, showing evidence of material re-heating to evaporation temperatures within the *vapor zone*[2] and *multi-phase*[3] zone in the plume above the keyhole during deep-penetration laser welding of both stainless steel and copper.

Despite considerable research on the plume's impact on laser welding, previous measurement techniques using transversally aligned probe beams have limitations, as they integrate attenuation effects across the entire path of the probe beam, including both the caustic of the processing beam and the areas to either side of it. This limitation was noted by Michalowski et al. [1], who addressed the issue by introducing a tilted probe beam close to the processing laser beam axis. Their work demonstrated that vapor plume-induced attenuation could result in a $>$ 4 % loss of laser power at a wavelength of 1030 nm. Uspenskiy et al. employed a coaxial probe beam to qualitatively demonstrate the presence of particles or droplets within the laser caustic by capturing scattered light from these particles with a spectrometer [3].

To address the limitations of previous methods, which do not fully and exclusively capture the attenuation effects along the path of the processing laser beam, we introduced a coaxial probe beam. This new approach enables direct measurement of attenuation solely along the axis of the processing laser beam, providing an accurate and quantitative assessment of laser beam attenuation caused by the plume during full-penetration laser welding. The experimental work in this study involved welding stainless steel, an aluminum alloy, and copper while varying the plume height. For stainless steel, additional experiments were performed to investigate the effects of different air/argon mixtures at various pressures on beam attenuation. To contextualize the measurements, Mie-theory calculations of single-particle interactions were performed and compared with the experimental results.

2. Experimental set-up

The experimental setup used to measure the attenuation of the laser beam in the plume of vapor and particles is shown in Fig. 1. This setup was used in sets of experiments where different materials were welded using process parameters chosen to achieve full-penetration welds. These parameters ensured that the keyhole was at least temporarily open on the bottom side of the sheet, as shown in Fig. 1.

The processing beam was provided by a fiber-coupled TruDisk 16002 laser with a wavelength of $\lambda_{\mathrm{proc}} = 1030$ nm. The fiber had a core diameter of 400 µm. Using focal lengths of $f_{\mathrm{proc,coll}} = 150$ mm for collimation and $f_{\mathrm{proc,focus}} = 400$ mm for focusing, produced a focus diameter of 1.07 mm on the surface of the sample. The processing was performed at normal incidence. Different laser powers were systematically adjusted to achieve stable full-penetration welding at the respective feed rates, sheet thicknesses, and ambient atmospheres. For copper, a reduced sheet thickness of 2 mm was required to maintain a stable full-penetration keyhole with an open bottom outlet, which is necessary for the coaxial measurement configuration. This ensures that all materials are compared under equivalent full-penetration welding conditions, enabling consistent plume diagnostics.

The probe beam, delivered by an IntegratedOptics MatchBox laser operating at $\lambda_{\mathrm{probe}} = 1064$ nm, was aligned coaxially with the processing beam. The small wavelength difference between the processing and probe beams was chosen to ensure similarity of the beam-plume interaction while still allowing for separation of the two by dichroic beam splitters and spectral filters. Owing to the minor variation of the complex refractive index of the three investigated materials between 1030 nm and 1064 nm [24–30], the associated optical properties can be assumed to differ only negligibly within this spectral interval. The coaxial alignment was realized using a beam combiner with high reflectivity at $\lambda = 1030$ nm and high transmission at $\lambda = 1064$ nm. The lens collimating the probe beam had a focal length of $f_{\mathrm{probe,coll}} = 25$ mm and was focused by the lens with a focal length of $f_{\mathrm{foc}} = 400$ mm also used to focus the processing beam. This resulted in a probe beam focus with a diameter of approximately 170 µm. The probe beam was focused on the bottom side of the metal sheet, in order to minimize clipping of the beam by the keyhole walls. Due to the coaxial alignment and the similar wavelengths of the probe and processing beams, their interactions with the vapor and particles in the plume can be assumed to be comparable. This includes both scattering and absorption, which contribute to the attenuation of both beams.

After transmission through the keyhole in the interaction zone, both the residual processing beam and the probe beam were collimated again using a lens with a focal length of $f_{\mathrm{coll}} = 400$ mm. To separate the two beams, two dichroic beam splitters were used to deflect the processing beam towards beam dumps. To further remove residual light from the processing beam leaking through the beam splitters and to block any thermal emissions from the process, a longpass filter with a cut-on wavelength of $\lambda_{\mathrm{LP,cut\text{-}on}} = 1050$ nm followed by a bandpass filter with a passband at $\lambda_{\mathrm{BP,center}} = 1064$ nm and a bandwidth of 3 nm FWHM (Full Width at Half Maximum) were used.

The isolated probe beam was then directed into an integrating sphere with a photodiode set to an acquisition rate of 100 kHz. This setup allowed the acquisition of the relative power of the probe beam as it passed through the plume in the interaction zone along the same axis as the processing beam. For each experiment, a dark reference was

[1] Throughout this work, the more common term *attenuation* is used synonymously with *extinction*, as defined in the Mie theory [13]. In this context, these words represent the sum of scattering and absorption, both of which contribute to the removal of light from the original beam path.

[2] The vapor zone refers to the region of the plume within the laser beam caustic, close to the beam focus, that is composed almost entirely of gaseous metal, containing a negligible amount of particles or droplets [22]. The presence of vapor is identified by atomic line emission, while scattering effects within this zone can be considered negligible.

[3] The multi-phase zone refers to the region of the plume within the laser beam caustic where both particles and vapor co-exist. In this region, scattering is non-negligible and becomes increasingly dominant with increasing particle content. By definition, the upper boundary of the multi-phase zone corresponds to the transition at which atomic line emission is no longer observed, and thus vapor is no longer present [22].

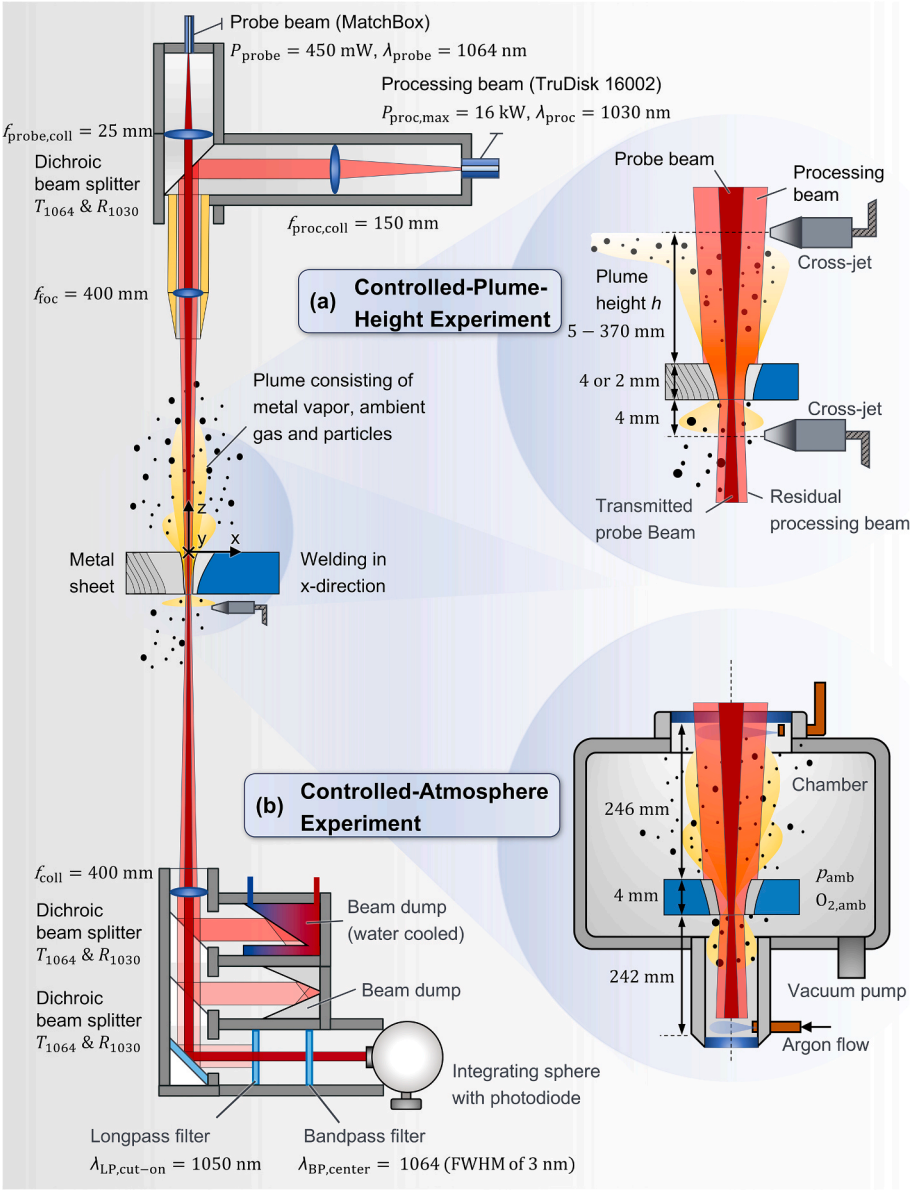


Fig. 1. Schematic diagram of the experimental setup used to measure the attenuation of a probe beam within the plume consisting of metal vapor, ambient gas, and particles during full-penetration welding. Controlled-Plume-Height Experiment (a): The plume was removed at varying heights. Controlled-Atmosphere Experiment (b): Different ambient pressures and residual oxygen contents were applied.

recorded immediately before welding, when the moving metal sheet temporarily blocked the probe beam, and was subsequently subtracted from the raw signal. To identify the relative transmission, the corrected signal was normalized by dividing it by a reference signal acquired prior to the start of each experiment. The use of the integrating sphere ensured that the measurement remained robust against beam pointing instabilities.

In the Controlled-Plume-Height Experiment (a), a high-pressure air cross-jet was used to remove the plume above the weld zone at various heights, as shown in Fig. 1. A second cross-jet was used to remove the plume and spatter below the sheet. In the Controlled-Atmosphere Experiment (b), a chamber was introduced to perform welds under different atmospheric conditions. This chamber was equipped with a vacuum pump to reduce the ambient pressure. To protect the windows through which the processing and probing beams passed, a small flow of Argon was introduced. Over time, as the chamber pressure was adjusted, the concentration of argon was increased, allowing for varying levels of residual oxygen. These oxygen levels were monitored with a lambda probe. The specific process parameters used in the (a) Controlled-Plume-Height Experiment and (b) Controlled-Atmosphere Experiment are shown in Table 1.

3. Results

The following sections cover signal processing (Section 3.1), the statistical evaluation of the probe beam's attenuation (Section 3.2), and the derivation of the extinction coefficient for different sections of the plume (Section 3.3).

3.1. Signal processing

Examining the photodiode signal from the relative power measurement, it is evident that the probe beam was not consistently transmitted throughout the entire welding process. High-speed imaging from previous experiments revealed fluctuations in the melt on the keyhole walls, which sometimes caused the bottom opening of the keyhole to

Table 1
Parameters used in the Controlled-Plume-Height Experiment (a) and Controlled-Atmosphere Experiment (b) as depicted in Fig. 1. Laser powers were adjusted to achieve full penetration; for copper, stable full-penetration with an open keyhole was only possible for 2 mm sheets.

Material	Feed rate	Laser power	Sheet thickness	Plume height h (above sheet)	Plume height (below sheet)	Ambient gas	Ambient pressure	Residual oxygen	Molar density O_2
–	m/min	W	mm	mm	mm	–	hPa	ppm	mol/m^3
Controlled-Plume-Height Experiment (a)									
Stainless steel (1.4301)	2	5750	4	$5 \leq h \leq 370$(in 8 steps)	4	Air	1000	210,000	8.62
Aluminum (EN AW 5083)	2	9000	4	$5 \leq h \leq 370$(in 8 steps)	4	Air	1000	210,000	8.62
Copper (Cu-ETP)	2	12,000	2	$5 \leq h \leq 370$(in 8 steps)	4	Air	1000	210,000	8.62
Controlled-Atmosphere Experiment (b)									
Stainless steel (1.4301)	1	5000	4	246	242	Air	1000	210,000	8.62
Stainless steel (1.4301)	1	5000	4	246	242	Air, Argon 5.0	1000	1100	0.0451
Stainless steel (1.4301)	1	5000	4	246	242	Air, Argon 5.0	100	2500	0.0103
Stainless steel (1.4301)	1	5000	4	246	242	Air, Argon 5.0	10	10,000	0.0041
Stainless steel (1.4301)	1	5000	4	246	242	Air, Argon 5.0	1	100,000	0.0041

temporarily close. Additionally, spatter ejected from the weld zone could partially or fully block the probe beam. These factors explain the sudden drops in the raw signal in Fig. 2a.

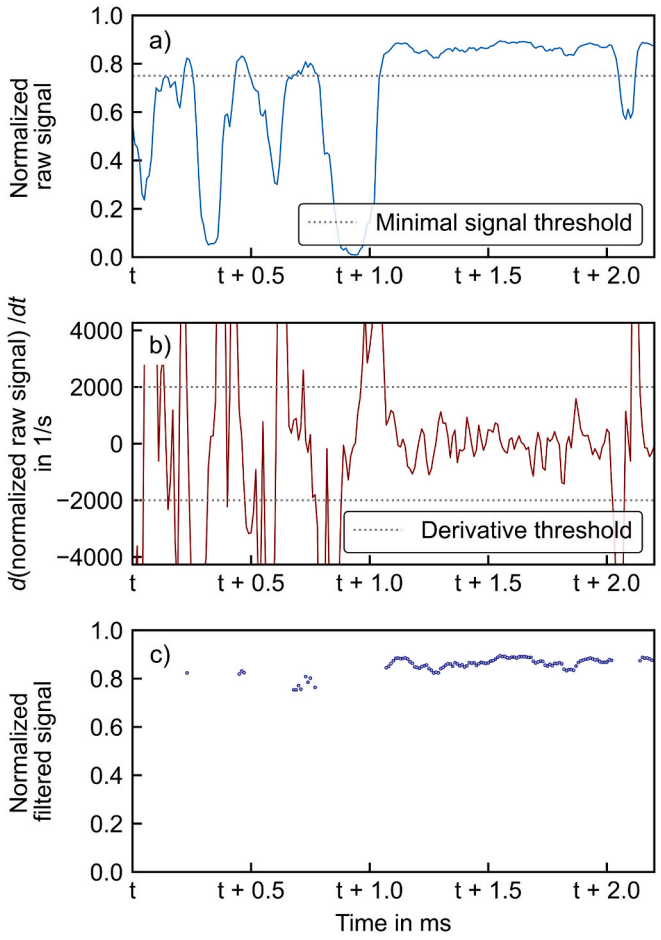


Fig. 2. Excerpts of the photodiode signal within the integrating sphere during welding of stainless steel (1.4301) at 5.75 kW and 2 m/min feed rate: a) normalized raw signal, b) first time derivative of the raw signal, and c) filtered signal.

In this research, we focus solely on the extinction that is directly relevant to the welding process, hence the attenuation occurring above the lower surface of the welded metal sheet. To minimize the influence of the attenuation occurring below the workpiece in the Controlled-Plume-Height Experiment (a), the plume and spatter below the metal sheet were removed using a cross-jet positioned as close as possible to the sheet without disturbing the process itself. Nevertheless, occasional blockage of the probe beam due to spatter or keyhole fluctuations may occur and needs to be considered in further data analysis.

To filter out the relevant data from the raw signal, and excluding the blockage events mentioned above, we applied a two-step filtering process. First, we introduced a minimal signal threshold, see Fig. 2a, set at 75 %, well below any attenuation levels of the plume reported in the literature. Second, data points where the absolute value of the first time derivative of the normalized raw signal exceeded 2000 s^{-1} were removed, as shown in Fig. 2b. This time derivative threshold was determined through an iterative process, ensuring that variations around the chosen value had minimal impact on the resulting filtered signal. This filter effectively removes rapid fluctuations in the signal, such as those caused by spatter particles passing through the probe beam. The combination of these two filters ensures that irrelevant data points are excluded from the raw signal, see Fig. 2c, preparing it for subsequent statistical analysis. During this data preparation process, it was confirmed that statistical values, including the median, 25th percentile, and 75th percentile, remained robust against variations in both the minimal signal threshold and the first time derivative threshold value.

3.2. Evaluation of the beam attenuation

Due to the filtering of the photodiode signal described in Section 3.1, the residual data can be assumed to represent beam attenuation caused by the vapor and particles in the plume, rather than by keyhole collapses or spatter blocking the beam. For statistical analysis of the extinction of the probe beam, several metrics were derived from the filtered photodiode signal and are presented as box-plots for comparison. A signal segment of the steady-state welding process lasting 750 ms was used from each experiment to calculate the statistical parameters shown in Fig. 3 through Fig. 7. The dashed red line represents the median, the blue box represents the interquartile range (IQR – 25th to 75th percentile),

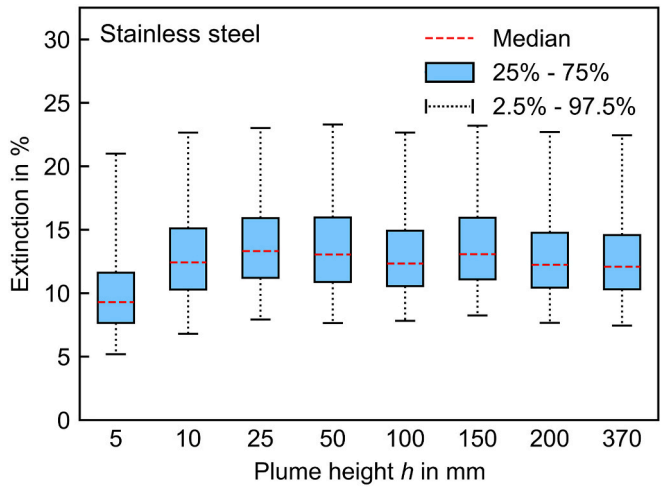


Fig. 3. Box-plots showing the attenuation of the probe beam during full-penetration welding of stainless steel (1.4301) in the Controlled-Plume-Height Experiment (a), see Fig. 1a. All calculated statistical values can be found in the Appendix.

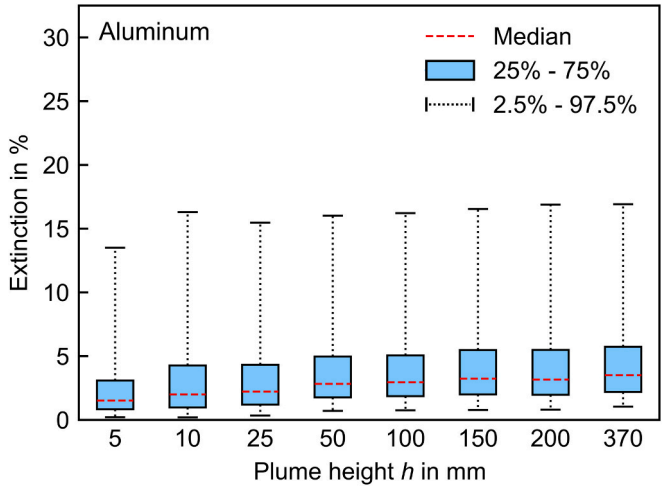


Fig. 4. Box-plots showing the attenuation of the probe beam during full-penetration welding of aluminum (EN AW 5083) in the Controlled-Plume-Height Experiment (a), see Fig. 1a. All calculated statistical values can be found in the Appendix.

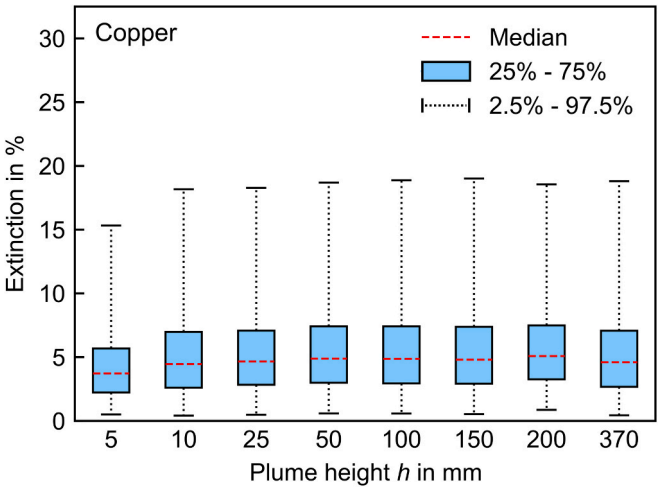


Fig. 5. Box-plots showing the attenuation of the probe beam during full-penetration welding of copper (Cu-ETP) in the Controlled-Plume-Height Experiment (a), see Fig. 1a. All calculated statistical values can be found in the Appendix.

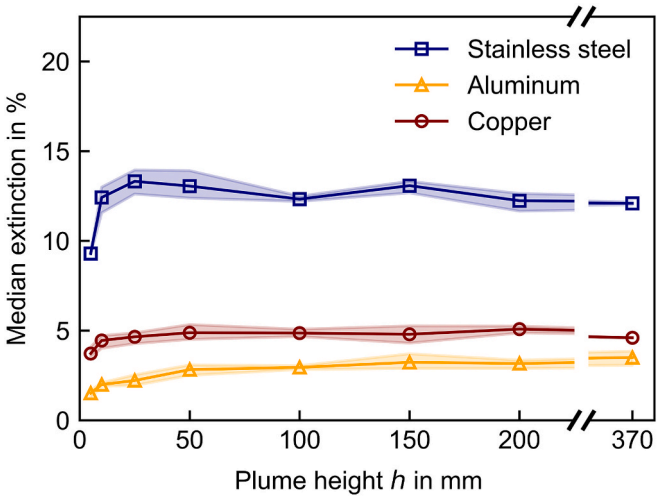


Fig. 6. Median attenuation of the probe beam as a function of the plume height during full-penetration welding of steel, aluminum, and copper, as illustrated by the box plots in Fig. 3 to Fig. 5. The shaded region represents the range between the lowest and highest medians across the three repetitions of each material's weld.

and the dotted black lines (whiskers) represent the 2.5th and 97.5th percentiles. In the Controlled-Plume-Height Experiment (a), each weld was repeated three times, with statistical values averaged over these repetitions. Fig. 3 through Fig. 5 each contain eight box-plots corresponding to specific plume heights. Fig. 6 summarizes the median values from these figures. In this context, “plume height” refers to the position of the upper cross-jet, see Fig. 1, which means there was no plume interacting with the beam above this height.

Fig. 3 presents the attenuation of the probe beam during the welding of stainless steel (1.4301). The leftmost box plot shows the extinction accumulated in the beam path from 5 mm above the metal sheet to 4 mm below it, with a median extinction of approximately 9.5 %. The interquartile range (IQR) of the extinction spans from 8 % to 12 %. The whiskers of the box plot indicate that extinction values range from as low as 5 % to as high as 20 % at the 2.5th and 97.5th percentiles, respectively. This indicates a relatively large fluctuation in the attenuation of the probe beam. It is assumed that not all of this power is lost to the process, as absorption and scattering by the vapor and particles within, or near, the keyhole may still contribute to heating the process zone. The second box plot, for a plume height of 10 mm, shows a significant increase in beam attenuation, compared to the plume height of 5 mm, up to a median of about 12.5 %. The further measurements, for plume heights of 25 mm and above, show no appreciable further increase in beam attenuation, which remains relatively constant at a median of approximately 13 $\pm$ 1 %. This means that almost all of the attenuation of the laser beam occurs below a distance of 10 mm above the sheet.

Fig. 4 shows box-plots of the extinction of the probe beam in the plume determined for welds in aluminum (EN AW 5083). Again, the box-plot with the 5 mm plume height shows the extinction of the beam from 5 mm above to 4 mm below the metal sheet, including the propagation through the keyhole. With a median value of approximately 2 %, the extinction of the beam is much lower than that for stainless steel. In the case of aluminum, the extinction increases gradually with increasing plume heights, indicating continuous attenuation along the length of the plume. The fluctuations in attenuation level, as indicated

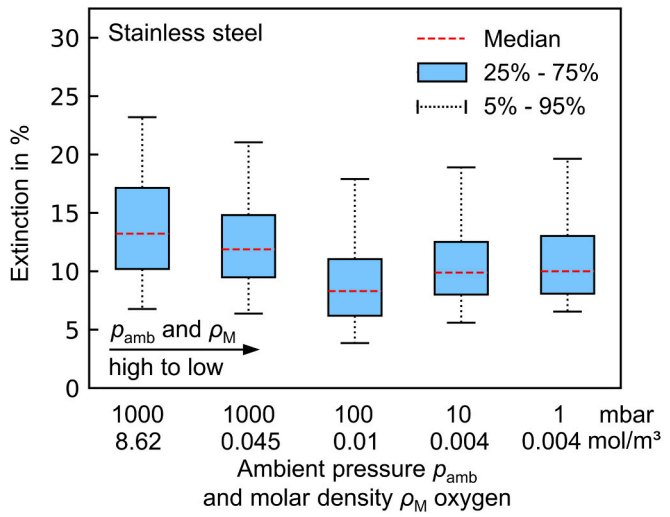


Fig. 7. Box-plots showing the attenuation of the probe beam during full-penetration welding of stainless steel in the Controlled-Atmosphere Experiment (b). The oxygen content and ambient pressure were varied, as described in Fig. 1b. All calculated statistical values can be found in the Appendix.

by the interquartile range (IQR), are of a similar order of magnitude to those observed for stainless steel.

The box-plots in Fig. 5 display the extinction of the probe beam in the plume during the welding of copper (Cu-ETP). At a plume height of 5 mm, the extinction for copper is approximately 3 %, positioning it between the values observed for stainless steel and aluminum. It should be noted that the copper samples had a thickness of 2 mm, i.e., half that used for stainless steel and aluminum, which may influence the absolute attenuation level. However, all materials were operated in a full-penetration regime, so the observed differences reflect plume behavior under comparable welding conditions rather than identical thermal geometries. As also observed for stainless steel, the attenuation does not significantly increase for plume heights above 10 mm.

Fig. 6 shows an overview of the median extinctions of the probe beam as presented in Fig. 3 to Fig. 5. The shaded region around each data point represents the range of median extinction values obtained from the three experimental repetitions.

Fig. 7 shows the extinction of the probe beam in the Controlled-Atmosphere Experiment (b) as a function of ambient pressure and residual oxygen content, measured with the experimental setup presented in Fig. 1b. For clarity, the oxygen content in parts per million (ppm) takes into account the ambient pressure, which results in a molar density (mol/m^3). This better accounts for the oxygen molecules available per volume for oxidation reactions which could occur in the process plume. The full set of welding parameters is listed in Table 1.

The two left-most box plots, comparing the same ambient pressure with standard and low oxygen content, reveal a small decrease in median beam attenuation from approximately 13.2 % to 11.9 % with the reduction of oxygen levels from 8.62 mol/m^3 to 0.045 mol/m^3. This represents a relative reduction of 10 % of the amount of laser beam energy absorbed and scattered by the plume. This trend continues as the oxygen content is reduced to 0.01 mol/m^3, at the same time as the overall gas pressure is reduced to 100 mbar. Further reductions in pressure and oxygen content result in a slight increase in attenuation.

3.3. Extinction coefficient

The results presented above enable the estimation of average extinction coefficients as a function of distance from the keyhole within the plume, as shown in Table 2. This estimation is obtained by calculating the difference in median extinction values between two plume heights from Fig. 3 to Fig. 5 and dividing the result by the distance between those heights. Due to fluctuations in the plume during the welding process, experiments with higher plume heights can occasionally exhibit slightly lower extinction values than lower plume heights. As a result of this, the subtraction method results in negative extinction coefficients in certain regions above 25 mm, which are not physically meaningful in this context. Considering that the additional extinction beyond 25 mm is minimal for both stainless steel and copper, it is reasonable to approximate the extinction coefficient as near-zero in these zones, see Table 2.

Table 2
Calculated average extinction coefficients across different sections of the vapor plume.

Material Region	Average extinction coefficient From 5 mm above to 4 mm below the keyhole	10–5 mm above the keyhole	25–10 mm above the keyhole	370–25 mm above the keyhole
Unit	m^{-1}	m^{-1}	m^{-1}	m^{-1}
Stainless steel (1.4301)	7.15	6.24	0.60	~ 0
Aluminum (EN AW 5083)	1.16	0.96	0.15	0.038
Copper (Cu-ETP)	3.38	1.46	0.13	~ 0

4. Discussion

To facilitate a deeper understanding of the mechanisms behind laser beam attenuation in the metal vapor plume, it is essential to first establish a theoretical basis for how the beam interacts with particles of varying size and material. For this purpose, fundamental Mie theory calculations of single-particle interaction are presented in Section 4.1, offering insights into the relative contributions of absorption and scattering to the overall beam extinction (attenuation). These results serve as a foundation for the interpretation of the experimental findings and guide the subsequent discussion.

The following sections explore the various features of the process plume, including differences in particle size, oxidation state, particle concentration, and their respective impact on the attenuation of the laser beam. Section 4.2 examines the extinction characteristics of the lower and upper parts of the plume, referred to as the vapor zone and particle zone in [22]. Section 4.3 addresses material-specific differences in attenuation behavior, including oxidation. Section 4.4 discusses the influence of the ambient atmosphere, considering both the surrounding gas composition and pressure. Finally, Section 4.5 provides further insights into whether absorption or scattering within the plume is the dominant mechanism contributing to the overall attenuation of the laser beam.

4.1. Mie calculations of single particle interaction

The Mie theory is used to calculate the scattering, absorption, and extinction of light by spherical particles using Maxwell's equations, providing exact solutions for these phenomena [13,31]. Calculations for a single scattering event require the particle diameter, the wavelength of the light, and the complex refractive index $m = n + ik$ of the particle, where n is the real part of the refractive index and k is the extinction coefficient. To transfer this from a single interaction event to the whole plume, one would need the local particle density and size distribution, as well as the optical properties of particles at every place in the caustic. Additionally, the complex refractive index of metal particles depends on temperature, phase state (solid or liquid), and oxidation level. However, reliable temperature-dependent refractive indices are generally not available in the literature, and the values are expected to vary during processing, as shown in [22,23]. Nevertheless, to estimate qualitative

trends in particle scattering and absorption, room-temperature refractive-index values were used to calculate the scattering and absorption characteristics of single particles.

Table 3 provides an overview of complex refractive indices for the main alloy elements of the welded materials and their corresponding oxides from existing literature. Using these complex refractive indices, the cross sections for the scattering, absorption, and extinction, as a function of the particle size, are calculated for the welded materials and their oxidized counterparts, using the Python implementation of the Mie theory of Prahl [32]. In Mie theory, the cross sections represent the effective areas over which a single particle removes energy from an incident plane wave through scattering and absorption, and their sum, extinction. These calculated cross sections are shown in Fig. 8 to Fig. 10. In the case of copper oxide, the literature is scarce and no calculations were conducted.

The inset plot in Fig. 8 shows a non-linear increase in the extinction cross section with increasing particle diameter up to approximately 100 nm for both Fe and Fe_3O_4. In this size range, extinction is dominated almost entirely by absorption, with scattering being negligible. Consequently, the single-scattering albedo, defined as the ratio of scattering to total extinction [31], is near zero for particles in this range. Above particle diameters of approximately 300 nm, the extinction cross section increases more linearly. In this larger size range, scattering becomes the primary contributor to extinction for both Fe and Fe_3O_4. Despite the dominance of scattering above 300 nm, absorption remains significant for both oxidized and non-oxidized particles. Overall, the difference in extinction cross section between Fe and Fe_3O_4 nanoparticles of the same size remains relatively minor throughout the investigated size range.

For aluminum, see Fig. 9, the extinction behavior similarly exhibits a non-linear increase in the extinction cross section for particle diameters below approximately 100 nm, consistent with the trends observed for Fe and Fe_3O_4. Above about 300 nm, the extinction cross section increases approximately linearly. However, compared to steel, the transition from absorption-dominated to scattering-dominated extinction occurs at smaller particle diameters. In this larger size range, particles larger than several hundred nanometers exhibit extinction dominated almost entirely by scattering for both Al and Al_2O_3, resulting in albedo values approaching unity. Notably, for particle diameters up to approximately 450 nm, Al exhibits substantially higher extinction than Al_2O_3.

Copper, shown in Fig. 10, exhibits a comparable extinction behavior, characterized by a non-linear increase in extinction cross section at small particle diameters, followed by a near-linear increase at larger sizes. For particles with diameters in the range of several hundred nanometers, extinction is again dominated almost entirely by scattering, with single-scattering albedo values approaching unity, similar to the behavior observed for aluminum.

4.2. Attenuation in the lower and upper plume

Reviewing Fig. 3 to Fig. 6 from the Controlled-Plume-Height

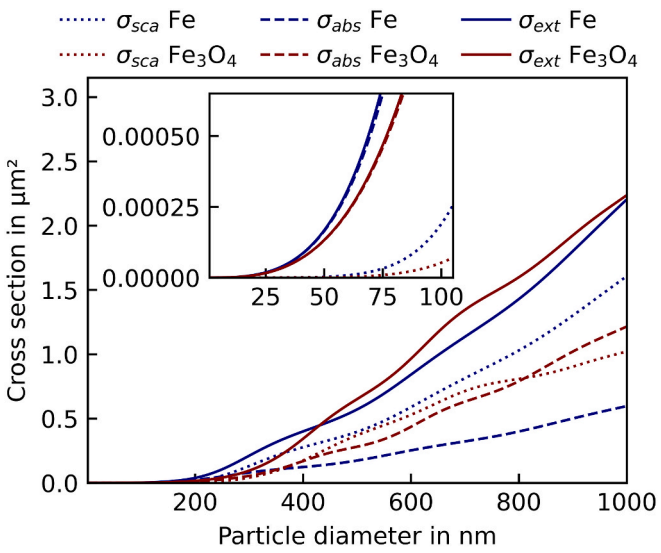


Fig. 8. Cross sections (in μm^2) calculated by the Mie theory for scattering (σ_{sca}), absorption (σ_{abs}), and extinction (σ_{ext}) of Fe and Fe_3O_4 nanoparticles as a function of the diameter (in nm). The calculations assume a complex refractive index of m = 2.958 + 3.998i for Fe and m = 2.111 + 0.37i for Fe_3O_4 at a wavelength of 1064 nm.

Experiment, the first key observation is that the laser beam experiences the highest extinction levels within and just above the keyhole for all three materials. This is probably because the density of particles or vapor is highest in this region. As the plume exits the keyhole, it spreads out into the space between the weld zone and the laser optics, reducing its concentration and thus reducing the overall beam attenuation. However, a common misconception is that the intense laser beam clears its path by rapidly evaporating any particles, leading to low extinction in areas with high laser intensity. As noted by Hansen and Duley [21], high-intensity laser radiation can indeed drive a continuous cycle of nucleation, condensation, and re-evaporation. Their calculations indicate that, under their specified conditions during welding of iron, this cycle process results in an extinction coefficient of 2.7 m^{-1} even within the keyhole. Applying Lambert-Beer's law, this corresponds to a 2.7 % loss of laser energy per centimeter. This theoretical estimation is of the same order of magnitude as the extinction coefficients measured in our study, as presented in Table 2. Consequently, these findings support the hypothesis that a dense aerosol of particles within, and just above, the keyhole significantly reduces laser power. However, it remains uncertain whether all of the energy absorbed by the condensing clusters or particles within the keyhole is lost to the welding process. Some of it may be transferred to the weld zone through condensation on the keyhole walls.

The upper plume, where particles are likely to be agglomerated, does not cause significant beam attenuation, regardless of the welded

Table 3
Complex refractive indices (*n* and *k*) of the main alloy elements in the welded materials and their oxide counterparts. Values are sourced from literature; however, actual values may vary depending on temperature, aggregate state, and lattice structure.

Material	Chemical formula	Wavelength in nm	Refractive index (n)	Extinction coefficient (k)	Reference
Iron	Fe	1064	2.9585	3.9977	Johnson, 1974 [24]
Iron	Fe	1064	3.235	4.3218	Ordal, 1985 [25]
Iron	Fe	1064	2.9216	4.3608	Querry, 1985 [26]
Iron sesquioxide, Iron(III)-oxide, Hematite	α-Fe_2O_3	1064	2.7542	0.011	Querry, 1985 [26]
Iron(II,III)-oxide, Magnetite	Fe_3O_4	1064	2.1112	0.3698	Querry, 1985 [26]
Aluminum	Al	1064	1.3763	10.245	Rakić, 1995 [27]
Aluminum	Al	1064	1.0286	9.2524	McPeak, 2015 [28]
Aluminum oxide, Sapphire	α-Al_2O_3	1064	1.726	0.0186	Querry, 1985 [26]
Aluminum oxide, Sapphire	α-Al_2O_3	1064	1.7545	~ 0	Malitson, 1972 [29]
Copper	Cu	1064	2.887	9.369	Werner, 2009 [30]

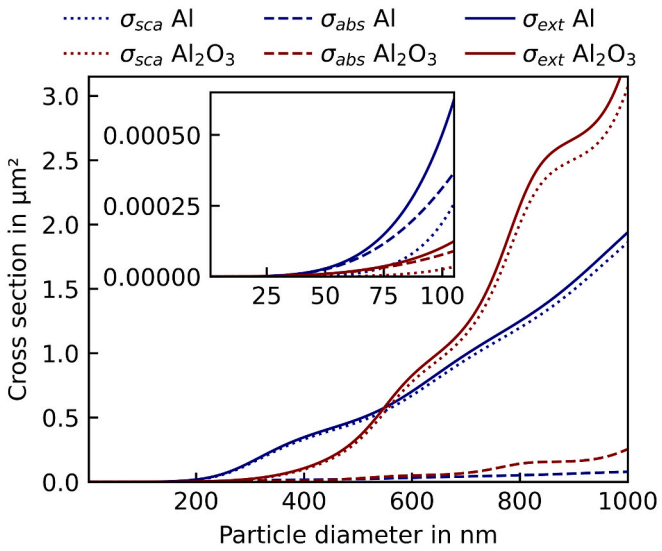


Fig. 9. Cross sections (in μm^2) calculated by the Mie theory for scattering (σ_{sca}), absorption (σ_{abs}), and extinction (σ_{ext}) of Al and Al_2O_3 nanoparticles as a function of the diameter (in nm). The calculations assume a complex refractive index of m = 1.376 + 10.245i for Al and m = 1.726 + 0.019i for Al_2O_3 at a wavelength of 1064 nm.

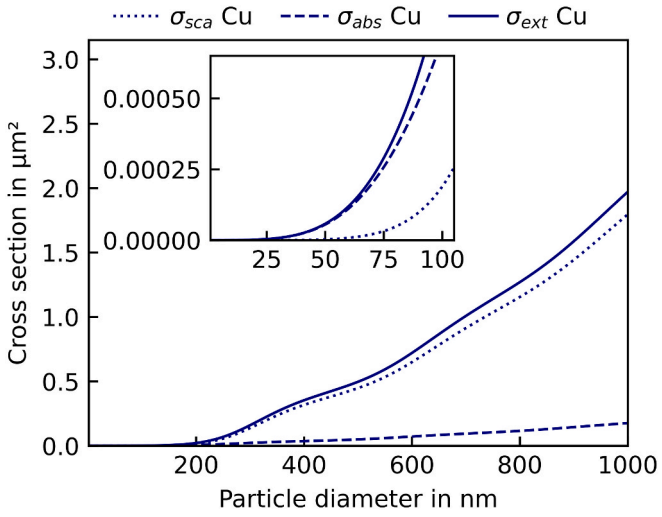


Fig. 10. Cross sections (in μm^2) calculated by the Mie theory for scattering (σ_{sca}), absorption (σ_{abs}), and extinction (σ_{ext}) of Cu nanoparticles as a function of the diameter (in nm). The calculations assume a complex refractive index of m = 2.887 + 9.369i for Cu at a wavelength of 1064 nm.

material. Examination of the calculated extinction cross sections presented in Fig. 8 to Fig. 10 for particles with diameters of several hundred nanometers reveals that these cross sections are approximately five orders of magnitude greater than those for particles with diameters of only a few tens of nanometers. This, in turn, leads to the conclusion that the particle number density in the upper plume must be very low to account for the minimal beam attenuation observed. This is consistent with the expected behavior of metal vapor and particles that disperse widely after ejection from the keyhole.

4.3. Material-dependent attenuation

When comparing the extinction box-plots for the different materials under the present welding parameters from Fig. 3 through Fig. 5 of the Controlled-Plume-Height Experiment, along with the respective extinction coefficients listed in Table 2, it is evident that the plume generated during welding of stainless steel leads to a significantly higher beam attenuation than is the case for copper, which in turn attenuates the beam more than aluminum. Several factors could explain this difference:

Additionally, differences in thermophysical properties, such as heat capacity, thermal conductivity, and vaporization behavior, affect how the laser beam interacts with the base material and consequently influence vapor generation. Optical properties, particularly the absorptivity of the base material, also play an important role. However, establishing a quantitative relationship between these material properties and the resulting beam attenuation is challenging because plume attenuation is governed by a sequence of strongly coupled processes, including absorption, melt pool and keyhole dynamics, evaporation, vapor ejection, nanoparticle formation, and subsequent oxidation. Furthermore, detailed information about the keyhole geometry, local pressure gradients, and vapor mass flow is not available, particularly for the Controlled-Atmosphere Experiment. These uncertainties make it difficult to accurately determine the amount of vapor ejected from the keyhole and, consequently, to establish a direct link between individual material properties and the observed attenuation.

Although a quantitative attribution is currently not possible, the Mie calculations for single-particle interactions presented in Section 4.1 provide insight into the material-dependent trends in plume extinction. Comparison of the extinction cross sections for particles with diameters below 100 nm, as shown in the inset plots of Fig. 8 to Fig. 10, reveals that iron particles are responsible for significantly higher attenuation than copper particles, which in turn attenuate more strongly than aluminum particles. This trend holds true for both pure metal particles and their oxidized forms. This correlates well with the observed differences in attenuation within the lower plume (and keyhole), see Fig. 6, during welding of stainless steel, copper, and aluminum.

It should be noted, however, that the extinction behavior of nanoparticles cannot be directly inferred from the absorptivity of the corresponding bulk material. For particle diameters well below the laser wavelength, scattering and absorption depend non-linearly on particle size and complex refractive index, see Section 4.1. Consequently, higher bulk absorptivity does not necessarily result in proportionally higher plume attenuation. Furthermore, the optical properties of nanoparticles change during cooling and oxidation, while their oxidation state, size distribution, and high-temperature refractive indices remain largely unknown. Therefore, a quantitative separation of the contributions of material absorptivity and thermophysical properties to the measured attenuation is not currently possible. The Mie calculations are thus primarily used to identify qualitative trends and assess consistency with the observed attenuation behavior.

Oxidation of nanoparticles also influences attenuation due to changes in the complex refractive index and thus optical material properties, see Table 3. Examination of the inset plots in Fig. 8 and Fig. 9 shows that, for nanoparticles in the tens-of-nanometers size range, the extinction cross section decreases upon oxidation compared to that of the corresponding non-oxidized particles. This effect is particularly pronounced for aluminum and its oxide. In practice, oxidation also alters the particle density and, consequently, its size, as shown in [19] for Al and Al_2O_3. Under atmospheric conditions, rapid oxidation of these nanoparticles is expected during cooling [20,22,23]. In our previous work [23], we identified aluminum(II)-oxide (AlO) in the hot metal vapor in the immediate vicinity of the keyhole through its characteristic emission in spectrometer measurements. The formation of AlO represents an intermediate oxidation state that oxidizes further to Al_2O_3 [33]. The rapid oxidation of aluminum nanoparticles to Al_2O_3 therefore provides a plausible explanation for the significantly lower beam attenuation observed in the plume during aluminum welding compared to that of stainless steel and pure copper. Similar to AlO, the presence of FeO and CuO in their respective plumes was experimentally confirmed [23], indicating that steel and copper nanoparticles in the plume are also

likely to oxidize rapidly during condensation and solidification. For steel, however, the impact of oxidation on beam attenuation is not as pronounced as it is for aluminum, as discussed in Section 4.1. In the case of copper, missing refractive index data for its oxide prevented a comparison of oxidation effects with the other materials using Mie calculations.

4.4. Influence of the ambient atmosphere on the attenuation

The two leftmost box-plots from the Controlled-Atmosphere Experiment in Fig. 7 display attenuation measurements at constant pressure with varying oxygen content, showing that attenuation decreases with lower oxygen levels. Assuming that reduced oxygen content slows or even prevents oxidation, one could expect slightly higher attenuation, rather than lower, as indicated by the extinction cross sections of Fe and Fe_3O_4 shown in the inset plot of Fig. 8. However, variations in oxygen content can also induce competing effects on the attenuation by simultaneously influencing particle size, density and oxidation state. This can potentially counteract the attenuation changes expected from oxidation alone, which were discussed above in Section 4.3.

The same fundamental mechanisms affecting particle size, particle density, and oxidation state are likely present for all three investigated materials. However, the influence of oxidation on attenuation depends on the optical properties of the respective oxide species. For aluminum, oxidation substantially reduces the absorption efficiency and, consequently, the attenuation, as shown in Fig. 9. Therefore, suppressing oxidation under reduced-pressure or inert-gas conditions could contribute to increased attenuation during aluminum welding. In contrast, no such assessment can currently be made for copper, as reliable optical property data for the relevant copper oxides at the investigated wavelength are not available in the literature.

Under standard atmospheric conditions, typical particle sizes in the lower vapor plume range from a few nanometers to several tens of nanometers. For mild steel, particles are generally around 50 nm [34], whereas stainless steel welding produces smaller particles, typically in the range of 28–33 nm [35]. Under argon or helium atmospheres, mild steel particle sizes range from 10 - 30 nm [35]. Due to the non-linear extinction behavior of nanoparticles in this size range, as discussed in Section 4.1, a distribution of smaller particles results in a lower cumulative extinction cross section compared to a single, larger particle of equivalent mass [13,36]. This reduction in particle size could therefore explain the decrease in attenuation observed in Fig. 7.

Reducing the pressure of the air/argon mixture from 1000 mbar to 100 mbar resulted in a further decrease in median beam attenuation. This trend could again be attributed to a reduction in particle size, in this case associated with reduced ambient pressure. It has been shown that at very low pressures, particle diameters can decrease into the single-digit nanometer range [37]. However, the results presented in Fig. 7 show that further reductions in pressure to 10 and 1 mbar led to a slight increase in beam attenuation compared to 100 mbar. One possible contributing factor is increased metal vapor generation, since the boiling point decreases with decreasing ambient pressure [38]. At the same time, reduced pressure also modifies keyhole conditions, vapor expansion dynamics, and overall plume structure. In addition, changes in particle composition and oxidation states of alloying elements in stainless steel may further influence the optical response [20].

As these mechanisms act simultaneously and are strongly coupled, the individual contribution of increased vapor generation to the observed attenuation cannot be isolated. Only the resulting net effect is accessible in the present measurements.

4.5. Absorption versus scattering contributions to attenuation

From the attenuation measurements presented in Fig. 6 alone, it is not possible to distinguish between losses due to absorption and those due to scattering. However, the Mie calculations in Section 4.1 clearly demonstrate that extinction from particles in the tens-of-nanometers range, corresponding to particle sizes typically found in the lower plume, is dominated almost entirely by absorption. In this regime, the scattering albedo is close to zero. The only exception is aluminum, where both pure metal and oxidized particles exhibit non-negligible scattering even at these small sizes.

In the upper plume, particles are likely agglomerated and have sizes on the order of several hundred nanometers. In this size range, particles scatter a significant portion of light relative to the total extinction. This effect is particularly pronounced for copper and aluminum, where scattering dominates the extinction, resulting in a scattering albedo close to one. These findings align well with those reported in our previous study [23], where scattering and thermal emission along the beam axis were investigated for the same set of materials. In that work, the highest volume scattering efficiency was observed in the upper plume of aluminum, which is consistent with the Mie calculations presented here. Combined with the coaxial beam attenuation measurements reported in this study, these results enable further conclusions. Since aluminum exhibits the lowest overall beam attenuation among the three materials, and given that almost no attenuation was measured in the upper plume, it can be concluded that scattering contributes only a negligible amount to the total beam attenuation. As a further implication, the even lower scattering efficiency observed in the lower plume [23] indicates that light scattering by particles can be neglected as a mechanism for energy redistribution in or above the keyhole.

4.6. Interpretation and comparison with literature

Table 4 summarizes previously reported attenuation values for laser welding of different materials with NIR laser sources and allows the results of the present work to be placed into the context of existing literature. The reported literature values for steel exhibit a considerable spread. This variation can partly be attributed to differences in processing parameters, including laser wavelength, power, beam caustic characteristics, shielding atmosphere, and material alloy. Furthermore, the employed measurement approaches differ substantially, comprising off-axis transversal measurements, near-longitudinal measurements, and numerical simulations.

A fundamental advantage of the coaxial measurement approach presented in this work is that the probe beam follows the same optical path as the processing laser beam. Consequently, attenuation is measured directly along the processing beam path through the plume. In contrast, off-axis probe beam techniques sample only part of the plume and often cannot access the region immediately above the keyhole, where vapor densities are highest. As noted by Shcheglov [14], measurements several millimeters above the workpiece therefore underestimate the total attenuation. The coaxial configuration overcomes this limitation by directly measuring attenuation both within and immediately above the keyhole.

The attenuation values measured in this study should not be interpreted as universal quantities. As mentioned above, the exact values of laser beam attenuation are expected to depend on the employed processing conditions, including laser power, wavelength, focal position, beam caustic parameters, and ambient atmosphere. These parameters influence the rate of material evaporation, the resulting vapor density, and the balance between vapor reheating, condensation, and particle formation within the plume. Consequently, different welding conditions can lead to different attenuation levels. This dependence is also reflected by the literature data summarized in Table 4, where attenuation values vary considerably despite the use of similar NIR laser wavelengths. The observed scatter demonstrates that attenuation is sensitive to both process parameters and measurement methodology.

Nevertheless, the principal findings of the present work are expected to remain valid over a broad range of NIR laser welding processes. In particular, the spatial variation of attenuation along the plume and the material-dependent differences between stainless steel, aluminum, and

Table 4
Comparison of the laser beam attenuation by the vapor plume measured in the present study with experimental and model-based values reported in the literature.

Material	Laser power in kW	Attenuation in %	Wavelength of probe beam in nm	Method	Reference
Low-alloyed steel	20	12	1070	Off-axis transversal measurement	Shcheglov, 2013 [16]
Low-alloyed steel	5	5–13	1070	Off-axis, transversal measurement	Shcheglov, 2011 [14]
Mild steel	8	up to 40	1064	Off-axis, transversal measurement	Greses, 2004 [17]
Stainless steel (SUS304)	10	4	1070	Off-axis, transversal measurement	Kawahito, 2008 [39]
Stainless steel	3	> 4	1030	Off-axis, near longitudinal measurement	Michalowski, 2007 [1]
Stainless steel (1.4301)	5.75	10–15 (IQR), 13 (median)	1064	Coaxial measurement	Present work
Aluminum (AlMg3)	6	7	1070	Numerical model	Bachmann, 2026 [18]
Aluminum (EN AW 5083)	9	2–5 (IQR), 3 (median)	1064	Coaxial measurement	Present work
Copper	1.5 kW	1.9	980	Off-axis, transversal measurement	Kaufmann, 2021 [15]
Copper (Cu-ETP)	12	3–7 (IQR), 5 (median)	1064	Coaxial measurement	Present work

copper arise from fundamental plume interaction mechanisms that are expected to persist under different processing conditions. Although absolute attenuation values may vary, the underlying relationships between vapor generation, particle formation, absorption, and scattering are expected to remain qualitatively similar. The present results therefore provide insight not only into the investigated conditions but also into the fundamental mechanisms governing plume-induced laser beam attenuation in deep-penetration laser welding.

5. Conclusions

In this study, the extinction of a probe beam coaxially propagating with the processing laser beam through the process plume and welding keyhole during full-penetration welding of stainless steel, aluminum, and copper was measured for the first time. The measurements were conducted with varying heights of the plume and under different ambient atmospheric conditions. This provided insights into the details of the attenuation of the process beam as a function of distance from the keyhole as well as the influence of atmospheric pressure and ambient gas composition. The key findings of this study are as follows:

- During full-penetration welding, the laser beam experiences significant attenuation within the vapor plume and particle cloud.
- The measured median extinction under the parameters used here was approximately 13 % for stainless steel, 3 % for aluminum, and 5 % for copper at standard atmospheric conditions.
- The majority of attenuation occurs within and in the vicinity of the keyhole region.
- Scattering, which was found to be strongest in the upper regions of the plume [22,23], plays only a minor role in the overall beam attenuation.
- The dominant mechanism of attenuation is therefore absorption, which likely drives a cycle of nucleation, condensation, and re-evaporation in regions of high laser intensity, as previously proposed in [21].
- For stainless steel, lowering the oxygen content of the surrounding gas from 8.62 mol/m^3 to 0.045 mol/m^3 at atmospheric pressure reduced the median beam attenuation from 13.2 % to 11.9 %, likely due to a decrease in average particle size.
- Reducing the argon/air mixture pressure from 1000 mbar to 100 mbar decreased the median attenuation from approximately 11.9 % to 8.3 %, again probably as a result of smaller particle sizes.
- A further pressure reduction to 10 mbar and 1 mbar led to a slight increase in median attenuation to around 10 %, possibly caused by enhanced vapor generation due to the lower boiling point at such low pressures.

This study presents quantitative extinction measurements that support a detailed analysis of scattering and absorption mechanisms contributing to overall laser beam attenuation. These findings enhance the fundamental understanding of the underlying physical mechanisms and thus contribute to strategies for mitigating the adverse effects of the vapor plume on the welding process. In the future, this knowledge could facilitate the development of closed-loop control strategies for deep-penetration laser welding processes.

CRediT authorship contribution statement

Johannes Wahl: Writing – original draft, Visualization, Software, Methodology, Investigation, Formal analysis, Data curation, Conceptualization. **Christian Frey:** Writing – review & editing, Resources, Methodology, Investigation. **John Powell:** Writing – review & editing, Supervision, Methodology. **Simon Olschok:** Writing – review & editing, Funding acquisition. **Uwe Reisgen:** Funding acquisition. **Christian Hagenlocher:** Writing – review & editing, Supervision, Funding acquisition. **Thomas Graf:** Writing – review & editing, Supervision, Methodology, Funding acquisition, Conceptualization.

Declaration of competing interest

The authors declare that they have no known competing financial interests or personal relationships that could have appeared to influence the work reported in this paper.

Acknowledgements

The presented work was funded by the Deutsche Forschungsgemeinschaft (DFG, German Research Foundation) - project number: 463452146. Additionally, we acknowledge partial support from the InnovationCampus Future Mobility funded by the Baden-Württemberg Ministry of Science, Research and the Arts.

Appendix

Statistical data of extinction measurement

Table 5
Statistical data of the laser beam extinction by the vapor plume for different plume heights of the Controlled-Plume-Height Experiment (a).

Material	Corresponding figure	Plume height	Laser beam extinction						
			2.5th percentile	25th percentile (First quartile)	50th percentile (median)	75th percentile (Third quartile)	97.5th percentile	Average	Standard deviation
		mm	%						
Stainless steel (1.4301)	Fig. 3	5	5.20	7.66	9.30	11.62	21.00	10.18	3.78
		10	6.80	10.30	12.42	15.11	22.65	13.02	3.91
		25	7.93	11.21	13.32	15.92	23.02	13.87	3.75
		50	7.65	10.89	13.06	15.96	23.30	13.75	3.98
		100	7.83	10.57	12.33	14.92	22.66	13.14	3.69
		150	8.25	11.10	13.08	15.95	23.20	13.86	3.84
		200	7.67	10.44	12.24	14.76	22.70	13.01	3.71
		370	7.46	10.31	12.09	14.58	22.45	12.85	3.68
Aluminum (EN AW 5083)	Fig. 4	5	0.21	0.84	1.52	3.08	13.51	2.71	3.41
		10	0.19	0.97	1.99	4.27	16.30	3.46	4.05
		25	0.34	1.20	2.22	4.32	15.47	3.54	3.82
		50	0.71	1.76	2.82	4.97	16.02	4.11	3.82
		100	0.76	1.86	2.95	5.06	16.22	4.21	3.84
		150	0.77	2.00	3.23	5.48	16.54	4.50	3.94
		200	0.80	1.97	3.17	5.49	16.88	4.49	3.98
		370	1.04	2.19	3.50	5.74	16.92	4.73	3.94
Copper (Cu-ETP)	Fig. 5	5	0.50	2.22	3.72	5.68	15.33	4.56	3.66
		10	0.41	2.60	4.45	6.97	18.17	5.45	4.27
		25	0.48	2.83	4.65	7.08	18.28	5.60	4.25
		50	0.59	2.98	4.88	7.42	18.69	5.88	4.34
		100	0.57	2.94	4.86	7.41	18.88	5.89	4.40
		150	0.53	2.92	4.80	7.37	19.01	5.85	4.43
		200	0.86	3.27	5.08	7.49	18.56	6.02	4.19
		370	0.44	2.67	4.60	7.07	18.81	5.61	4.40

Table 6
Statistical data of the laser beam extinction by the vapor plume under different atmospheric conditions in the Controlled-Atmosphere Experiment (b).

Material	Corresponding figure	Ambient pressure	Molar density O_2	Laser beam extinction						
				2.5th percentile	25th percentile (First quartile)	50th percentile (median)	75th percentile (Third quartile)	97.5th percentile	Average	Standard deviation
		hPa	mol/m^3	%						
Stainless steel (1.4301)	Fig. 7	1000	8.6200	10.19	5.23	13.22	17.14	23.95	13.80	4.90
		1000	0.0451	9.48	5.54	11.88	14.81	22.79	12.50	4.27
		100	0.0103	6.19	3.34	8.30	11.04	20.54	9.14	4.21
		10	0.0041	8.01	4.97	9.90	12.51	21.26	10.69	3.97
		1	0.0041	8.08	6.12	10.01	13.02	21.92	11.08	4.02

Data availability

Statistical data are provided in the Appendix. Raw datasets generated during this study are available from the corresponding author upon reasonable request.

References

[1] A. Michalowski, A. Heß, A. Ruß, F. Dausinger, Plume attenuation under high power Yb:YAG laser material processing, in: Proceedings of Lasers in Manufacturing (LIM), Munich, AT-Fachverlag, Stuttgart, 2007.

[2] H. Hügel, T. Graf, Materialbearbeitung mit Laser, fifth ed., Springer Fachmedien Wiesbaden, Wiesbaden, 2023.

[3] S.A. Uspenskiy, P.Y. Shcheglov, V.N. Petrovskiy, A.V. Gumenyuk, M. Rethmeier, Spectral diagnostics of a vapor-plasma plume produced during welding with a high-power ytterbium fiber laser, Opt. Spectrosc. 115 (2013) 140–146, https://doi.org/10.1134/S0030400X13070205.

[4] Y. Kawahito, N. Matsumoto, M. Mizutani, S. Katayama, Characterisation of plasma induced during high power fibre laser welding of stainless steel, Sci. Technol. Weld. Join. 13 (2008) 744–748, https://doi.org/10.1179/136217108X329313.

[5] A. Matsunawa, J.-D. Kim, T. Takemoto, S. Katayama, Spectroscopic studies on laser induced plume of aluminum alloys, in, in: Proceedings of the International Congress on Applications of Lasers and Electro Optics (ICALEO), Laser Institute of America (LIA), 1995, pp. 719–728.

[6] R. Fabbro, M. Hamadou, F. Coste, Metallic vapor ejection effect on melt pool dynamics in deep penetration laser welding, J. Laser Appl. 16 (2004) 16–19, https://doi.org/10.2351/1.1642633.

[7] R. Fabbro, S. Slimani, I. Doudet, F. Coste, F. Briand, Experimental study of the dynamical coupling between the induced vapour plume and the melt pool for Nd–Yag CW laser welding, J. Phys. D Appl. Phys. 39 (2006) 394–400, https://doi.org/10.1088/0022-3727/39/2/023.

[8] J. Volpp, Impact of fume particles in the keyhole vapour, Appl. Phys. A 125 (2019), https://doi.org/10.1007/s00339-018-2346-2.

[9] F. Yang, X. Meng, S.N. Putra, A. Artinov, M. Bachmann, M. Rethmeier, Numerical analysis of the effect of an oscillating metal vapor plume on the keyhole and molten pool behavior during deep penetration laser beam welding, J. Laser Appl. 35 (2023) 042041, https://doi.org/10.2351/7.0001094.

[10] B. Zhu, R. Xiao, S. Xie, T. Liu, T. Huang, Coupled simulation of plume–keyhole interaction in laser deep penetration welding, Sci. Technol. Weld. Join. 30 (2025) 379–388, https://doi.org/10.1177/13621718251376847.

[11] Y. Kawahito, K. Kinoshita, N. Matsumoto, M. Mizutani, S. Katayama, Effect of weakly ionised plasma on penetration of stainless steel weld produced with ultra high power density fibre laser, Sci. Technol. Weld. Join. 13 (2008) 749–753, https://doi.org/10.1179/136217108X356971.

[12] T. Scholz, K. Dickmann, A. Ostendorf, Investigation of the formation of nanoparticles during laser remote welding, Phys. Procedia 41 (2013) 90–97, https://doi.org/10.1016/j.phpro.2013.03.055.

[13] H.C. de van Hulst, Light scattering by small particles, Unabridged and corrected republication of the work originally published in nineteenthfifthseventh by John Wiley & Sons, Inc., N.Y, Dover Publications Inc; LSC Communications, New York, 1957.

[14] P. Shcheglov, S.A. Uspenskiy, A.V. Gumenyuk, V.N. Petrovskiy, M. Rethmeier, V. M. Yermachenko, Plume attenuation of laser radiation during high power fiber laser welding, Laser Phys. Lett. 8 (2011) 475–480, https://doi.org/10.1002/lapl.201110010.
[15] F. Kaufmann, J. Ermer, A. Maier, S. Roth, M. Schmidt, Influence of plume attenuation under high power laser welding of copper using visible wavelengths, J. Laser Appl. 33 (2021) 042006, https://doi.org/10.2351/7.0000505.
[16] P.Y. Shcheglov, A.V. Gumenyuk, I.B. Gornushkin, M. Rethmeier, V.N. Petrovskiy, Vapor–plasma plume investigation during high-power fiber laser welding, Laser Phys. 23 (2013) 16001, https://doi.org/10.1088/1054-660X/23/1/016001.
[17] J. Greses, P.A. Hilton, C.Y. Barlow, W.M. Steen, Plume attenuation under high power Nd:yttritium–aluminum–garnet laser welding, J. Laser Appl. 16 (2004) 9–15, https://doi.org/10.2351/1.1642636.
[18] M. Bachmann, S.N. Putra, F. Yang, X. Meng, P. Pusbatzkies, M. Rethmeier, Elucidation of the laser beam energy attenuation by the vapor plume formation during high-power laser beam welding, J. Laser Appl. 38 (2026) 012001, https://doi.org/10.2351/7.0001863.
[19] C. Frey, J. Wahl, S. Olschok, C. Hagenlocher, T. Graf, U. Reisgen, Analysis of particles inside the metal vapor plume during laser beam welding in vacuum using a simplified multi-wavelength method, Vacuum (2026) 114964, https://doi.org/10.1016/j.vacuum.2025.114964.
[20] C. Frey, J. Wahl, K. Schmidt, S. Olschok, C. Hagenlocher, T.E. Weirich, T. Graf, U. Reisgen, Characterization of particles inside the metal vapor plume during laser beam welding in atmosphere and vacuum, Vacuum (2025) 113964, https://doi.org/10.1016/j.vacuum.2024.113964.
[21] F. Hansen, W.W. Duley, Attenuation of laser radiation by particles during laser materials processing, J. Laser Appl. 6 (1994) 137–143, https://doi.org/10.2351/1.4745348.
[22] J. Wahl, C. Frey, J. Powell, F. Zaiß, M. Haas, S. Olschok, U. Reisgen, C. Hagenlocher, T. Graf, Laser-plume interactions in deep-penetration remote laser welding of stainless steel, Opt. Laser Technol. 186 (2025) 112678, https://doi.org/10.1016/j.optlastec.2025.112678.
[23] J. Wahl, C. Frey, J. Powell, M. Haas, S. Olschok, U. Reisgen, C. Hagenlocher, T. Graf, Material-specific beam-plume interactions during deep-penetration laser welding of stainless steel, aluminum, and copper, J. Adv. Joining Process. 13 (2026) 100366, https://doi.org/10.1016/j.jajp.2025.100366.
[24] P. Johnson, R. Christy, Optical constants of transition metals: Ti, V, Cr, Mn, Fe, Co, Ni, and P, Phys. Rev. B 9 (1974) 5056–5070, https://doi.org/10.1103/PhysRevB.9.5056.
[25] M.A. Ordal, R.J. Bell, R.W. Alexander, L.L. Long, M.R. Querry, Optical properties of fourteen metals in the infrared and far infrared: Al, Co, Cu, Au, Fe, Pb, Mo, Ni, Pd, Pt, Ag, Ti, V, and W, Applied Optics, No, 1985, p. 24.
[26] M.R. Querry, Optical constants, Kansas City, Missouri, USA, 1985.
[27] A.D. Rakić, Algorithm for the determination of intrinsic optical constants of metal films: application to aluminum, Appl. Opt. 34 (1995) 4755–4767, https://doi.org/10.1364/AO.34.004755.
[28] K.M. McPeak, C.D. van Engers, S. Bianchi, A. Rossinelli, L.V. Poulikakos, L. Bernard, S. Herrmann, D.K. Kim, S. Burger, M. Blome, S.V. Jayanti, D.J. Norris, Ultraviolet plasmonic chirality from colloidal aluminum nanoparticles exhibiting charge-selective protein detection, Adv. Mater. 27 (2015) 6244–6250, https://doi.org/10.1002/adma.201503493.
[29] I.H. Malitson, Refractive index and birefringence of synthetic sapphire, J. Opt. Soc. Am. 48 (1958), https://doi.org/10.1364/JOSA.48.000072.
[30] W.S.M. Werner, K. Glantschnig, C. Ambrosch-Draxl, Optical constants and inelastic electron-scattering data for 17 elemental metals, J. Phys. Chem. Ref. Data 38 (2009) 1013–1092, https://doi.org/10.1063/1.3243762.
[31] G. Mie, Grundlagen einer Theorie der Materie, Ann. Phys. 344 (1912) 1–40, https://doi.org/10.1002/andp.19123441102.
[32] S. Prahl, miepython: pure python calculation of Mie scattering, Zenodo (2025).
[33] M.W. Beckstead, A Summary of Aluminum Combustion, Utah, USA, 2004.
[34] P. Ščeglov, Study of vapour-plasma plume during high power fiber laser beam influence on metals. Dissertation, Bundesanstalt für Materialforschung und -prüfung (BAM), Berlin, 2012.
[35] T. Scholz, Nanopartikelbildung beim Laserschweißen von Metallen, Dissertation, Bochum (2015).
[36] C.F. Bohren, D.R. Huffman, Absorption and scattering of light by small particles, Wiley paperback publ, Wiley, New York, 1998.
[37] A. Matsunawa, S. Katayama, A. Susuki, T. Ariyasu, Laser production of Metallic Ultra-Fine Particles, Trans. Joining Welding Res. Inst. Osaka (1986).
[38] C.S. Kim, Thermophysical properties of stainless steels, 1975.
[39] S. Oiwa, Y. Kawahito, S. Katayama, Optical properties of laser-induced plume during high power laser welding, in: Proceedings of International Congress on Applications of Lasers and Electro Optics (ICALEO), Laser Inst. of America (LIA), Orlando, Fla., 2009, pp. 359–365.